Taylor & Francis
Taylor & Francis Group

Mesoscale surface current fields in the Baltic Sea derived from multi-sensor satellite data

MARTIN GADE*†, BENJAMIN SEPPKE‡ and LEONIE
DRESCHLER-FISCHER‡

†Zentrum für Marine und Atmosphärische Wissenschaften (ZMAW), Institut für
Meereskunde, Universität Hamburg, 20146 Hamburg, Germany
‡Fachbereich Informatik, Universität Hamburg, 22527 Hamburg, Germany

We demonstrate the use of multi-sensor satellite images for the computation of mesoscale surface currents in the Northern and Southern Baltic Proper by enhancing and combining image-processing techniques. The sequential satellite images were acquired by the Thematic Mapper (TM), the ERS-2 Synthetic Aperture Radar (SAR), the Wide-Field Scanner (WiFS) and the Sea-viewing Wide Field-of-view Sensor (SeaWiFS) during extensive cyanobacterial blooms in July 1997 and in July/August 1999. We also used a pair of Advanced SAR (ASAR) images from May 2005 showing imprints of singular oil spills in the Southern Baltic Proper. Different marine surface films and accumulated algae at the water surface were taken as tracers for the local motion of the sea surface. Data from sensors working at different electromagnetic bands (e.g. TM and SAR) were used to apply high-speed feature-matching (cross-correlation) techniques for motion detection. The sufficiently short time lags between the multiple image acquisitions (from less than 1 h to approximately 1 day) and the high spatial coverage allowed for the calculation of optical flow (i.e. surface motion) fields, which include small-scale turbulent structures that are not resolved by operational numerical models. Our computed surface currents range from 4 to 35 cm s^{-1} and are generally larger than those provided by the numerical models for the same dates and areas. We attribute this difference to local wind forcing, causing higher drift velocities at the very sea surface, which is seen from space, but which is not resolved by the numerical models.

1. Introduction

Remote-sensing data from satellite-borne sensors working at the same or different electromagnetic frequencies can be used to derive ocean current fields, if the same features are visible in the different data sets and if the data were acquired quasi-simultaneously (i.e. within a certain time period, which depends on the lifetime of the observed features, the current speed and the sensors' spatial resolution). These features may be driven by the local surface motion, and the correlation of the two-dimensional data sets may therefore allow for the calculation of mesoscale ocean current fields.

---

*Corresponding author. Email: martin.gade@zmaw.de

The use of sequential satellite data for the computation of ocean current fields has been established since the mid-1980s, when the maximum cross-correlation (MCC) method was introduced by Emery *et al.* (1986). Optical images of the ocean surface from the Advanced Very High Resolution Radiometer (AVHRR) and the Coastal Zone Color Scanner (CZCS) were used to generate sea surface current maps off the California coast (Tokmakian *et al.* 1990). Further studies have demonstrated the strengths and limitations of this technique, when applied to ocean colour and thermal images (Garcia and Robinson 1989, Kamachi 1989, Emery *et al.* 1992, Bowen *et al.* 2002).

The application of the MCC method to derive sea ice motion from sequential synthetic aperture radar (SAR) imagery was first demonstrated by Collins and Emery (1988). Since then, further methods for the use of SAR imagery for sea ice tracking have been developed (e.g. Kwok *et al.* 1990, Li *et al.* 1998). However, only recently the use of sequential SAR imagery for ocean surface current estimates applying the MCC technique (Fiedler 2003, Gade *et al.* 2003) and wavelet analysis (Liu *et al.* 2006) was reported. Those studies have in common that they use imprints of marine surface films in SAR imagery, that is, dark patches that result from the damping of the small-scale surface waves responsible for the radar backscatter (Alpers and Hühnerfuss 1988).

While several studies have been performed on the use of single sensor types (i.e. either optical or radar) for the calculation of surface motion, the combined use of those sensors for sea surface current estimates has not sufficiently been demonstrated so far. Marine surface films are well suited for such kinds of data analyses, because they can change both the sea surface roughness (Gade *et al.* 1998a) and its emissivity of electromagnetic waves (Kahru *et al.* 1993), and may thus be visible on both radar and optical imagery.

The Baltic Sea is an almost fully enclosed non-tidal brackish water body of about 380 000 km^2. The summer (July–August) blooms in the open Baltic Sea are often dominated by the species *Nodularia spumigena* and *Aphanizomenon* spp. These blooms are usually associated with a massive appearance of marine surface films consisting of oily substances that are released by the algae. During the later phase of the bloom, the algae start to flocculate and accumulate on the sea surface in large quantities, thereby becoming visible even with non-optimized satellite sensors (see figure 1). The surface accumulations of cyanobacteria can cause a higher reflectance of near-infrared (NIR) radiation and in some cases can cause a local increase in the satellite-derived sea surface temperature (SST) due to increased absorption of sunlight by the higher phytoplankton pigment concentration (Kahru *et al.* 1993). Thus, multi-sensor satellite data are suitable for detecting and tracking algae blooms. Moreover, if a sufficient amount of satellite data is available, sea surface currents may be derived.

2. Satellite and meteorological data

In order to demonstrate the applicability of a multi-sensor approach, we used three sets of remote-sensing data acquired (1) in July 1997 over the Northern Baltic Proper, (2) in July/August 1999 over the Southern Baltic Proper and (3) in May 2005, again, over the Southern Baltic Proper. Most of the images are historical data, nonetheless they are very well suited for the basic analyses presented herein. The images were acquired by various satellite-borne sensors working in the optical, infrared and microwave bands. Figure 2 shows the central Baltic Sea (Baltic Proper) with the geographical locations of the used satellite data inserted.
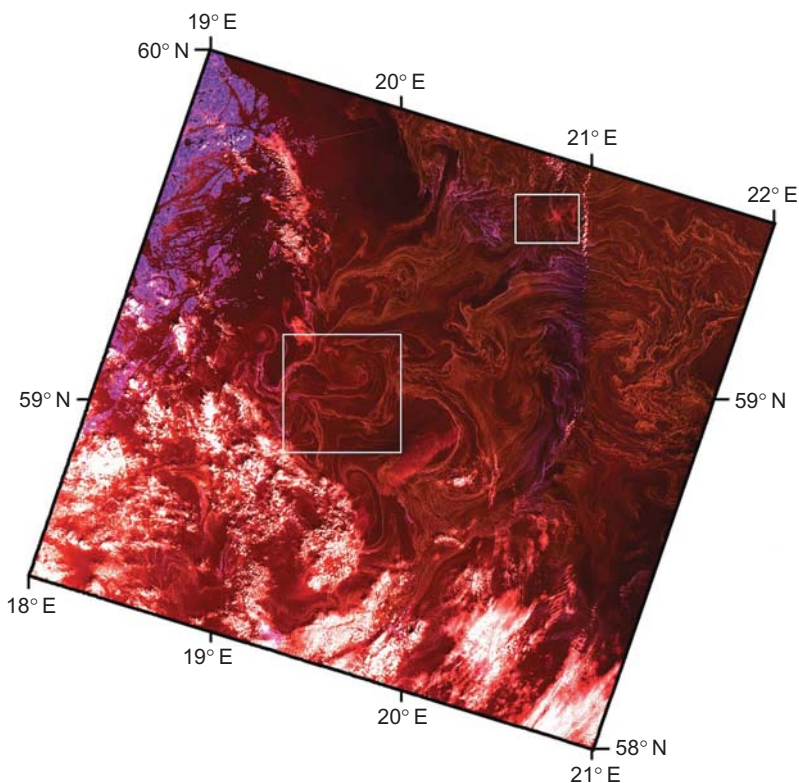
Figure 1. False-colour composite of TM bands 1, 2 and 4 showing manifestations of an ongoing algae bloom on 15 July 1997, in the Northern Baltic Proper. Bright patches in the lower half are clouds; blue patches on the left are the Swedish mainland and archipelago. The squares denote the location of subsets used for the surface motion calculation.

For the first study presented herein, the area of interest was the Northern Baltic Proper, north of the Swedish island of Gotland. On 15 July 1997, a day with extensive cyanobacterial blooms in the northern Baltic Proper, data from different satellite sensors were acquired over the same sea surface area. Among those sensors are the Thematic Mapper (TM) aboard Landsat, the SAR aboard ERS-2 and the Wide-Field Scanner (WiFS) aboard the Indian Remote-Sensing Satellite (IRS)-1C. The acquired data from these sensors have been used in the present study. A north-easterly wind of 3 m s^{-1} was reported on the Swedish island of Gotska Sandön, north of Gotland, on that day. The mean water surface temperature in the area was 18°C, with an inflow of colder (16°C) water from the north (Bothnian Sea) and the maximum temperature on 15 July 1997 on Gotska Sandön was 21.8°C. In figure 1, an RGB colour composite of Landsat TM bands 1, 2 and 4, respectively, is shown. The accumulated algae are visible as greenish structures in most parts of the image, blue colours result from land (the Swedish mainland and archipelago in the west and Gotska Sandön in the south) and white areas are clouds.

Another extensive cyanobacterial bloom was encountered in the Southern Baltic Proper, south of Gotland, in the late July/early August 1999. During about 1 week of mostly cloud-free weather conditions, more than 70 satellite images of that area
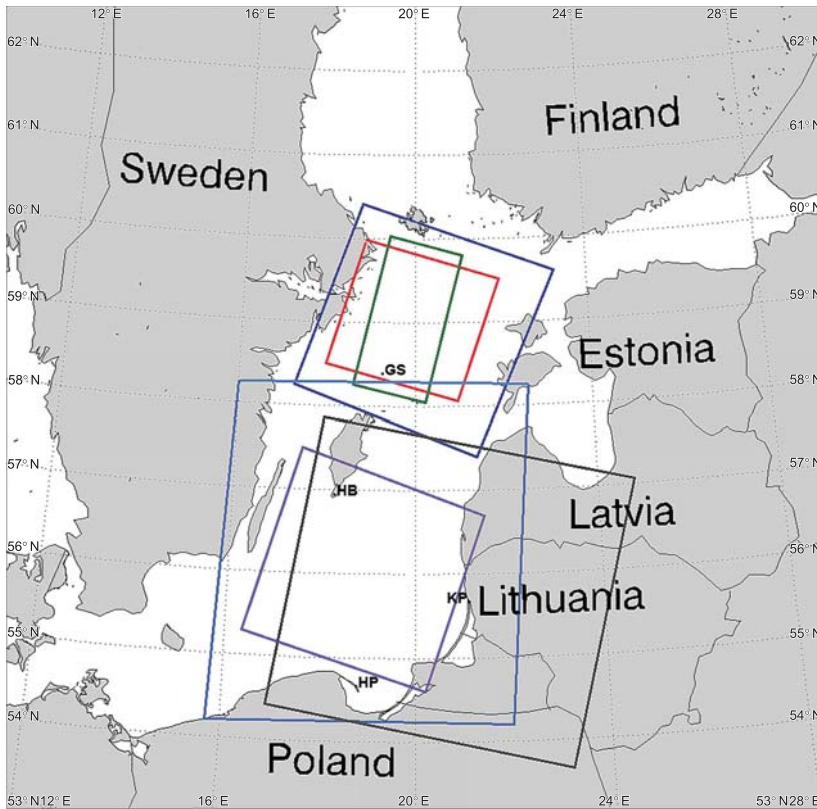
Figure 2. Map of the Central Baltic Sea (Baltic Proper) indicating the location of the used satellite images: 15 July 1997 (Northern Baltic Proper): SAR (green), Landsat TM (red) WiFS (dark blue); July/August 1999 (Southern Baltic Proper): WiFS (purple) and SeaWiFS (light blue); and 15 May 2005 (Southern Baltic Proper): two ASAR (both grey). The position of the weather stations is marked by GS (Gotska Sandön), HB (Hoburg), KP (Klaipeda) and HP (Hel Peninsula).

were acquired by a wealth of sensors working in the optical, infrared or microwave part of the electromagnetic spectrum. Among those are WiFS aboard IRS-1C and IRS-1D and the Sea-viewing Wide Field-of-View Sensor (SeaWiFS) aboard Sea Star. Both sensors work in similar spectral ranges and, thus, allow for using multi-sensor data without any constraint caused by the different imaging of the sea surface. For our second approach, which is based on the analysis of single sensor data, we used pairs of images from WiFS (acquired on 30 July) and from SeaWiFS (acquired on 1 and 2 August). In the late July or early August 1999, the mean surface temperature in the Southern Baltic Proper was 21°C, and a low westerly wind of 3 m s^{-1} and less was measured at weather stations in that area (e.g. in Hoburg on south Gotland and in Klaipeda, Lithuania).

The third set of analysed images was acquired by the Advanced SAR (ASAR) sensor (in Wide Swath mode) aboard the European Environmental Satellite (ENVISAT) on 15 May 2005. We detected two oil spills off the Bay of Gdansk that show up as irregular dark patches in these images. The mean water temperature in the spill area was 7°C, the air temperature was 10°C and a westerly wind of about 3 m s^{-1} was

Table 1. Satellite data and weather information.

| Sensor and data characteristics | | | | | Weather information | | | |
Sensor	Platform	Pixel size (m)	Date	Time (UTC)	Wind speed (m s^{-1})	Wind direction	Air temperature (°C)	Water temperature (°C)
Northern Baltic Proper								
TM	Landsat	30	15 July 1997	08:57	3	NE	21	18
SAR	ERS-2	12.5		09:47				
WiFS	IRS-1C	188		10:26				
Southern Baltic Proper								
WiFS	IRS-1C	188	30 July 1999	10:03	5	S	22	21
	IRS-1D			10:39				
SeaWiFS	Sea Star	1100	1 August 1999	11:03	<3	N–SW	24	21
			2 August 1999	11:47				
ASAR	ENVISAT	150	15 May 2005	09:00	3	W	10	7
				20:25				

measured on the Polish Hel Peninsula in the morning and evening of 15 May 2005 (i.e. at the times of the SAR image acquisitions), but raised up to 8 m s^{-1} during the daytime.

The different sensors, the satellite platforms, image pixel sizes and acquisition times are given in table 1, together with meteorological data from the closest weather stations. A more detailed description of the available data set can be found elsewhere (Gade *et al.* 1998b, Rud and Gade 1999, 2000).

3. Methods

The basic idea of the analyses presented herein is to derive motions of the observed brightness patterns (the so-called optical flow) as a proxy of the sea surface current field. Most of the analysed data show surface accumulations of algae and/or surfactants during ongoing algae blooms. Because of the small penetration depth in water of electromagnetic waves in the (far) red and NIR range, only features in the upper water layer can be detected in these channels. Thus, these bands were used for the computation of mean surface currents.

Depending on the sensors' imaging characteristics and of the amount of available data, we have applied different methods: a fast normalized cross-correlation analysis was performed with single-channel data from different sensors (working at different electromagnetic frequencies). A differential method based on the gradient (or optical flow) constraint equation (Horn and Schunck 1981) was used for series of multi-channel data acquired at the same electromagnetic bands and within a short period of time. In this article, we present examples for each of the methods.

In all cases, the mean velocity within an area of interest was determined as the arithmetic mean of all single motion velocities (i.e. the absolute values of the calculated current vectors). The standard deviation was derived accordingly.

3.1 *Global motion estimation*

Before any cross-correlation or differential image analysis was applied to the data, we corrected for the 'global motion' in the scene. The underlying idea is that the overall motion can be divided into two parts: a global (i.e. large-scale) motion describing the mean translation and rotation inside the entire scene; and a local (i.e. small to mesoscale) motion representing the deviation from that global movement. If the major part of the surface motion has already been corrected for in this early processing step, our approach allows reduction of both the size of the search window (i.e. the image fraction used for each processing step) of the normalized cross-correlation and the problem of large displacement distances, which is well-known in differential analysis.

For the estimation of the global displacement, we used an efficient implementation of the approach described by Sun (1996). We note that, if there is a major structural change of the scene elements, for example, a change in the overall surface film coverage, this method may fail to estimate a 'global motion'. In such a case, we have to expand the search window of the feature-matching approach and may be unable to get stable results from differential methods.

3.2 *MCC analysis*

We applied the 'Fast Normalized Cross-Correlation' method (Lewis 1995) to increase the performance of the normalized cross-correlation analysis. This method reduces the

computation time through the application of a Fast Fourier Transform and the use of lookup tables for the normalization of each cross-correlation. This type of image analysis was applied to pairs of images acquired by different sensors (i.e. one image per sensor), or for pairs of images acquired by the same sensor if the spatio-temporal changes were too large or if they were structural.

3.2.1 First case: 15 July 1997. The first example of surface currents derived by applying the MCC method was produced using TM data as shown in figure 1. The extensive algae bloom is visible through the imprints of algae surface accumulation in the TM colour composite. At the same time, an inflow of cold water from the Bothnian Sea in the north can be delineated through a tongue of algae-free water reaching into the imaged area. The two bright squares included in figure 1 denote the two areas for which surface currents were calculated.

Microwave (SAR) and NIR (TM band 4) data were used in this case because in both frequency bands the very water surface (or its roughness) is imaged and marine surface films can clearly be delineated. Both images were geo-coded and re-sampled to a pixel size of 30 m, and the SAR image was inverted, thus showing the surface films as bright patches similar to those in the TM image. Note that advanced differential approaches cannot be used in this case, because there is no grey value equivalence between the imaged objects in the different data sets.

As a first step, and in order to reduce the overall processing time, we have applied to the TM image a monotonicity operator (Enkelmann *et al.* 1988) that detects areas of strong algae accumulations as local maxima of the image brightness (monotony classes 7 and 8). The TM scene was chosen, because it was acquired prior to the SAR image (see table 1). The global motion was then estimated as 0° rotation and 17 and 6 pixels translation in horizontal and vertical directions, respectively. Thus, the underlying global motion was 18 cm s^{-1} in easterly direction (64°).

After the correction for the estimated global motion, we derived the two-dimensional cross-correlation for each detected feature in the TM image by correlating the surrounding 60 pixels × 60 pixels area with the corresponding part of the SAR image (100 pixels × 100 pixels). The local maximum of this correlation denotes the most likely (relative) location of the respective feature in the second (SAR) image and was used to determine the local motion vector.

A typical example of the results of this analysis is shown in figure 3. The green structures in the background origin from the TM scene, whereas the dark magenta patches origin from the SAR scene. Included in this figure are arrows that represent the local surface current as the superposition of the global motion and the local motion. The arrows are mostly parallel and denote a mean surface speed of 18 ± 2 cm s^{-1} in westerly direction.

3.2.2 Second case: 15 May 2005. Series of satellite images showing imprints of singular sea surface features may also be used to derive local surface currents through an MCC analysis. In order to demonstrate this, we have used a pair of ENVISAT ASAR Wide Swath-Mode images acquired on 15 May 2005 over the south-eastern Baltic Sea (Southern Baltic Proper). Figure 4 shows a composite of the two scenes acquired at 09:00 UTC and 20:25 UTC. The white rectangle in figure 4 denotes the location of the enlarged 82.5×60 km^2 area, where two oil spills have been detected in both images as dark irregular patches.
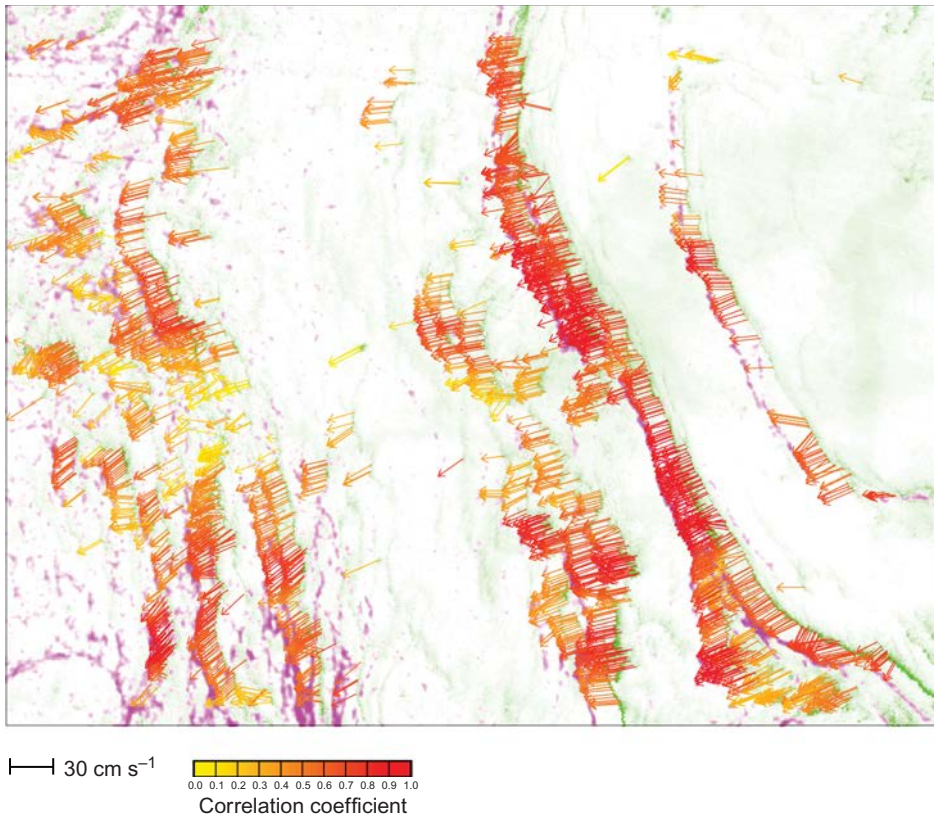
Figure 3. Result of the cross-correlation analysis applied to the TM4 and the SAR scene (see the small square in figure 1): features visible in the TM4 scene (green) are spatially shifted in the (inverted) SAR scene (dark magenta) by the local current. Image dimensions are 19.5 km × 15 km.

In order to identify those features, for which the cross-correlation method would be used, we have first calculated the gradient magnitude of the first SAR image using Gaussian derivatives (at scale $\sigma = 3.0$). We then applied a monotonicity operator (monotony classes 7 and 8), which detects the oil spill borders as local maxima of the image gradient.

After the feature detection in the first SAR image (acquired at 09:00 UTC), we calculated the two-dimensional cross-correlation of the surrounding 50 pixels × 50 pixels area of each detected feature point and the corresponding, but larger (230 pixels × 230 pixels), part of the second SAR image (acquired at 20:25 UTC). Again, the local maximum of this correlation was used to determine the surface motion vectors. Due to the strong structural change of the oil spills, we were not able to apply the global motion estimation in this case.

Our results of this analysis are shown in figure 5. The cyan patches in the background origin from the ASAR image acquired at 09:00 UTC, whereas the magenta patches origin from the ASAR image acquired at 20:25 UTC. The arrows are mostly parallel and denote mean surface speeds between 20 ± 2 cm s^{-1} (eastern spill) and 32 ± 1 cm s^{-1} (western spill).
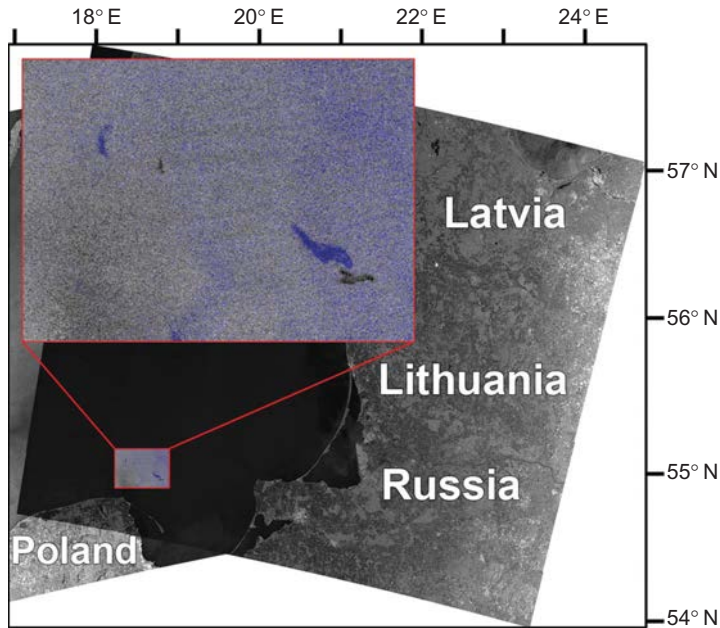
Figure 4. Composite of two SAR images of the Baltic Proper acquired on 15 May 2005. Image dimensions are approximately 950 km × 935 km. The white rectangle near the Bay of Gdansk denotes the (82.5 km × 60 km) part of the image used for the correlation analysis, see text. Dark patches show the oil spills in the first image, whereas the blue patches denote the spills in the second image.

3.3 Differential method

The differential method used herein is based on the optical flow constraint equation (Horn and Schunck 1981), which assumes that the image intensity of the scene elements does not change over time:

$$I(x, y, t) = I(x + \partial x, y + \partial y, t + \partial t), \tag{1}$$

where $I(x,y,t)$ is the image intensity of pixel $(x, y)^T$ at time t. Using the chain rule for differentiation, we get the common notation of the optical flow constraint equation:

$$I_x u + I_y v + I_t = 0, \tag{2}$$

where we introduced $u = \partial x$ and $v = \partial y$ for each pixel's motion in x- and y-directions, and $I_x = \partial I / \partial x$, $I_y = \partial I / \partial y$, $I_t = \partial I / \partial t$ for the partial derivatives.

Let $\nabla I = (I_x, I_y)^T$ be the gradient of the image I and $w = (u, v)^T$ the motion vector of each pixel. Then equation (2) simplifies to

$$\nabla I \cdot w + I_t = 0. \tag{3}$$

It is obvious that the two components of the motion cannot be uniquely derived from this single equation. One way to solve this commonly known aperture problem is to
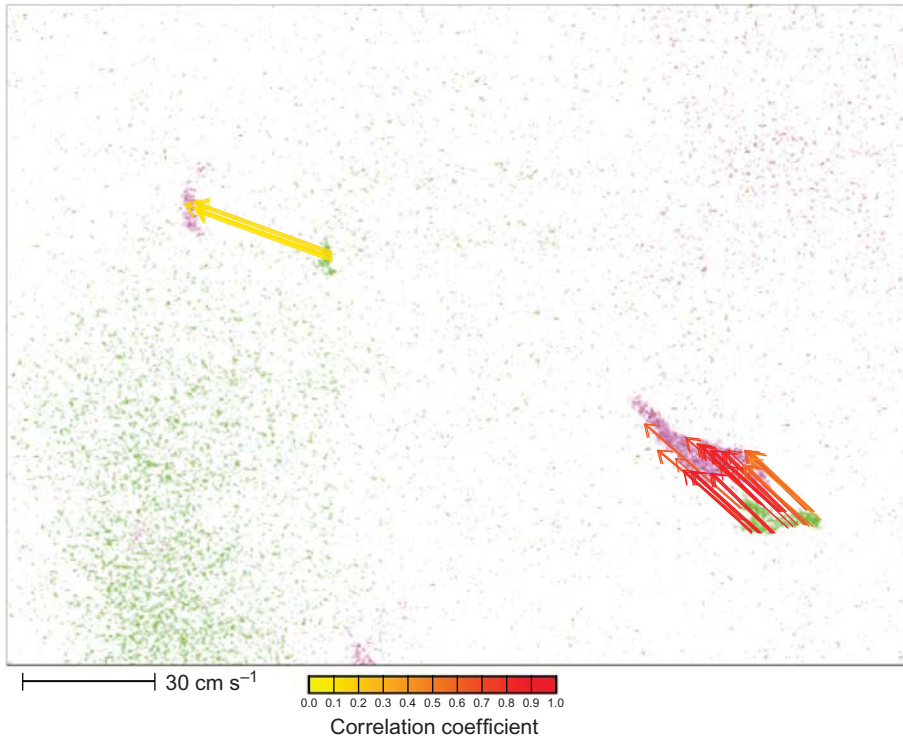
Figure 5. Result of the cross-correlation analysis applied to the SAR scene shown in figure 4: the oil spills of the first image at 09:00 UTC (green) are spatially shifted in the second image at 20:25 UTC (dark magenta) by the local current. Image dimensions are 82.5 km × 60 km.

use a pair of images for each point of time, for example, two images of the same spot that were acquired quasi-simultaneously at different electromagnetic bands. However, earlier experiments (Gade *et al.* 2003) have shown that this approach tends to produce motion artefacts that probably do not represent the real surface currents.

Another approach to solve the optical flow constraint equation is to add additional constraints to the basic equation. Lucas and Kanade (1981) assumed a constant motion within a given neighbourhood, NH, around each pixel. By adding this constraint, the former underdetermined equation becomes over-determined. Using a least square fit method, as proposed by Lucas and Kanade (1981), results in the following linear equation system:

$$\begin{pmatrix} \sum_{\mathrm{NH}} I_x^2 & \sum_{\mathrm{NH}} I_x I_y \\ \sum_{\mathrm{NH}} I_x I_y & \sum_{\mathrm{NH}} I_y^2 \end{pmatrix} \cdot w = - \begin{pmatrix} \sum_{\mathrm{NH}} I_x I_t \\ \sum_{\mathrm{NH}} I_y I_t \end{pmatrix}. \tag{4}$$

The approach of Horn and Schunck (1981) is slightly different, because they do not assume a constant motion in some neighbourhood but a smoothness of the motion within a given weight α. This assumption leads to a minimization of the motion gradient. Thus, Horn and Schunck (1981) proposed to minimize the (convex) functional:

$$E = \int (\nabla I \cdot w + I_t)^2 + \alpha \nabla^2 w, \tag{5}$$

which results in a solution of the corresponding Euler–Lagrange equations. This can be done iteratively:

$$w^{n+1} = \text{avg}(w^n) - \frac{\nabla w \cdot \text{avg}(w^n) + I_t}{\alpha^2 + I_x^2 + I_y^2}, \tag{6}$$

where avg(w^n) denotes the local motion average of step n, which has been computed by means of the arithmetic mean. The advantage of this minimization process is that in those parts of the image, where the image gradient diminishes, motion estimates are 'filled-in' from their neighbourhood motion. This is necessary to avoid a lack of information in these areas and to fulfil the constraint of a smooth motion.

The approach of Horn and Schunck (1981) can be seen as a global approach, because it determines motion by minimizing a global energy functional, while the approach of Lucas and Kanade (1981) is local and its locality is determined by the size of the chosen neighbourhood, NH.

Assuming the real current motion to be both smooth and global, we used an adapted version of the algorithm described by Horn and Schunck (1981). To avoid numerical instabilities, we replaced the calculation of the spatial gradients by a convolution with a first order Gaussian filter kernel with a given standard deviation σ. This avoids artefacts due to high spatial gradients caused by noise. Additionally, we replaced the proposed local average method used during the iteration process by a convolution with a Gaussian filter kernel (with the same given standard deviation σ).

3.3.1 First case: 15 July 1997. A first example of surface currents derived using the differential method was obtained using two images acquired on 15 July 1997, by the TM and WiFS sensors (see figure 2). We chose a sub-scene close to that used for the cross-correlation analysis (see the larger square in figure 1). Given the imaging properties (i.e. the reflectance) of the detected features were not changing significantly within the period of both image acquisitions (89 min, see table 1), pairs of images acquired by the two sensors at corresponding electromagnetic bands could be used for the differential method. The images were acquired at corresponding spectral bands (0.63–0.69 μm and 0.62–0.68 μm for TM band 3 and WiFS band 1, respectively) and were geo-coded and re-sampled at the lower spatial resolution (188 m). We applied the extended Horn and Schunck algorithm with a Gaussian filter's standard deviation $\sigma = 1.0$, a smoothing factor $\alpha = 2.0$ and with 200 iterations.

The resulting vector field is shown in figure 6. At first glance, the most pronounced results are accumulations of strong current vectors in the northwest and southwest corners of figure 6. However, these patterns result from clouds that were present in the first image but not in the second image and are, thus, artefacts of the applied method.

3.3.2 Second case: July/August 1999. In July and August 1999, most parts of the sea surface in the Southern Baltic Proper were covered by algae accumulations (Rud and Gade 2000). The comprehensive data set acquired over that area between 27 July and 2 August comprises WiFS and SeaWiFS satellite imagery that is suitable for applying
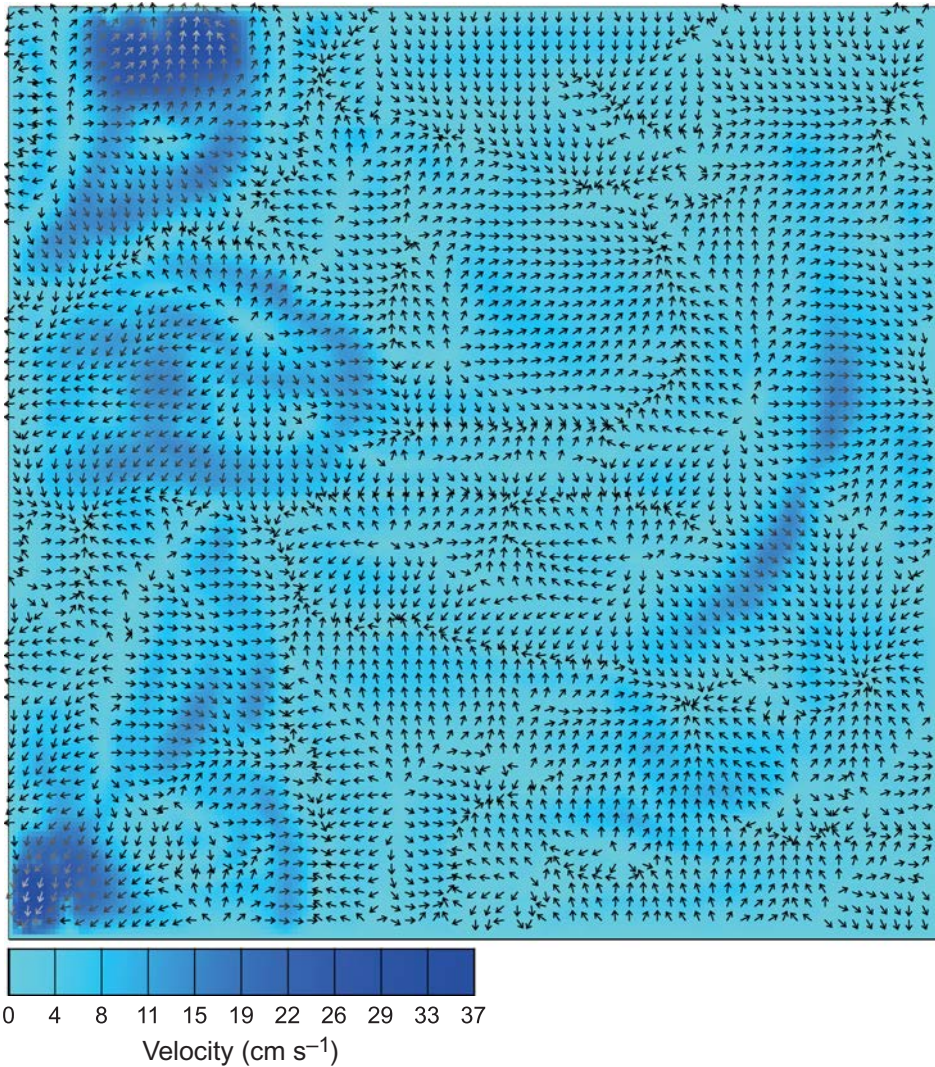
Figure 6. Result of the application of the differential method using pairs of TM and WiFS scenes (see the lower square in figure 1) acquired on 15 July 1997 in the Northern Baltic Proper. Image dimensions are 37.6 km × 37.6 km.

the differential method. From this data set, we have chosen two pairs of multi-channel satellite images for our analyses.

The composite of the two WiFS images acquired on 30 July 1999, at 10:03 UTC and 10:39 UTC is shown in figure 7. From both acquisitions, band 1 (0.62–0.68 μm) was used for our analyses. The light grey irregular patches in most parts of the image are caused by surface accumulations of cyanobacteria. Because of the short time lag between the two acquisitions (36 min) and the spatial resolution of the WiFS sensors (188 m), the minimum surface velocity that can be resolved with this data set is about 2–3 cm s^{-1}, which is a realistic value for minimum currents.
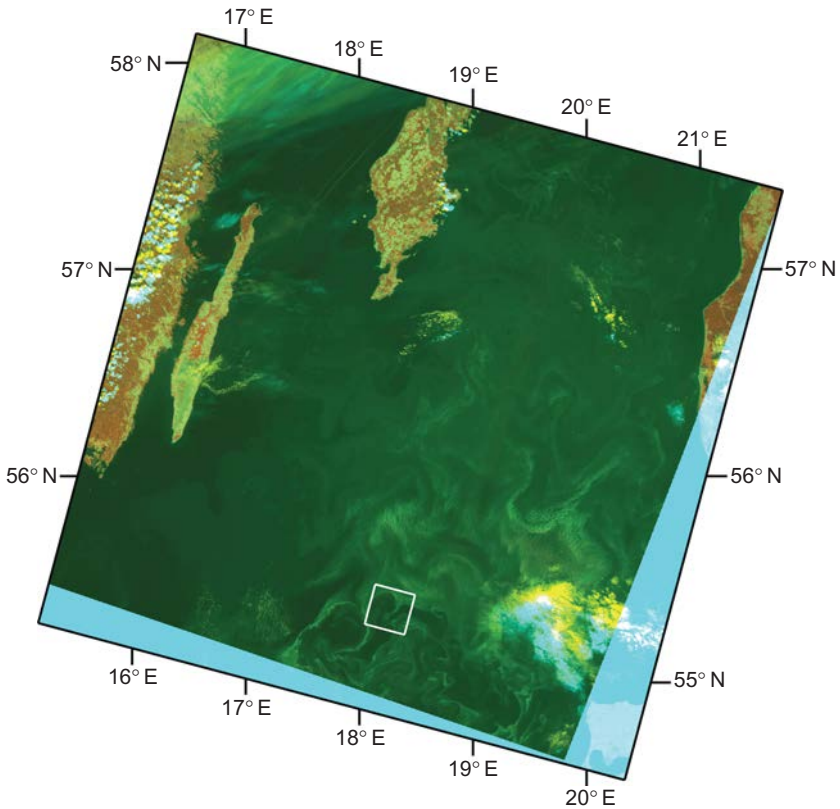
Figure 7. Composite of two WiFS images of the Southern Baltic Proper acquired on 30 July 1999, at 10:03 UTC and 10:39 UTC. The image dimensions are 265 km × 265 km, the southern tip of Gotland and the coast of Latvia are visible in the upper left part and in the upper right corner, respectively. The white square denotes the subsection used for the differential analysis, see text.

For the calculation of the surface current fields we applied the extended Horn and Schunck (1981) algorithm with a Gaussian filter's standard deviation $\sigma = 1.0$. In order to avoid artefacts in the calculated currents that result from grey value changes in the images and that do not reflect motions, we used a higher smoothing factor $\alpha = 5.0$. As in the previous case, we performed 200 iterations. The result of the differential analysis is shown in figure 8. In areas where the algae caused pronounced signatures, we calculated realistic surface currents of about 25–35 cm s^{-1}.

3.3.3 Third case: August 1999. Finally, we used a pair of SeaWiFS images acquired on 1 and 2 August 1999, to investigate whether low-resolution satellite imagery, acquired on consecutive days, is also suitable for calculating mean sea surface currents. Figure 9 shows a composite of the NIR channels 7 and 8 of the August-1 SeaWiFS scene (0.745–0.785 µm and 0.845–0.885 µm, respectively) and of channel 7 of the August-2 scene (0.745–0.785 µm). The white square inserted into
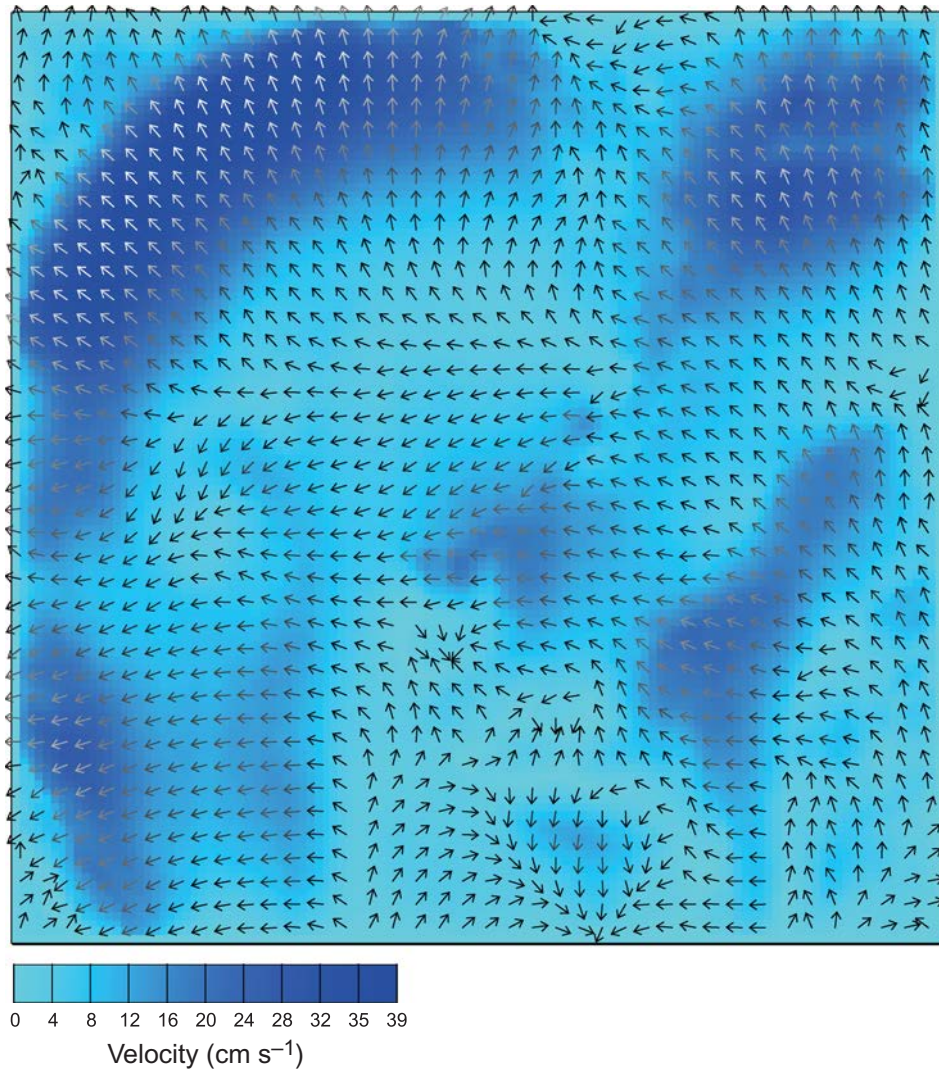
Figure 8. Surface motion field derived with the differential method using a pair of WiFS images acquired on 30 July 1999, shown in figure 7. The area dimensions are 22.5 km × 22.5 km.

figure 9 denotes the 100×200 km^2 area for which sea surface currents were calculated. For this calculation we applied the adapted Horn and Schunck (1981) algorithm to band 5 of both acquisitions using a Gaussian filter's standard deviation $\sigma = 1.0$. Because of the longer time lag between the two image acquisitions (1 day), a higher smoothing factor $\alpha = 20.0$ had to be chosen. Again, we performed 200 iterations.

The results of our analysis of the SeaWiFS data presented in figure 10 are different from those presented before, as the (daily) mean currents calculated using this data set are considerably lower and range from only 4 to 10 cm s^{-1}.
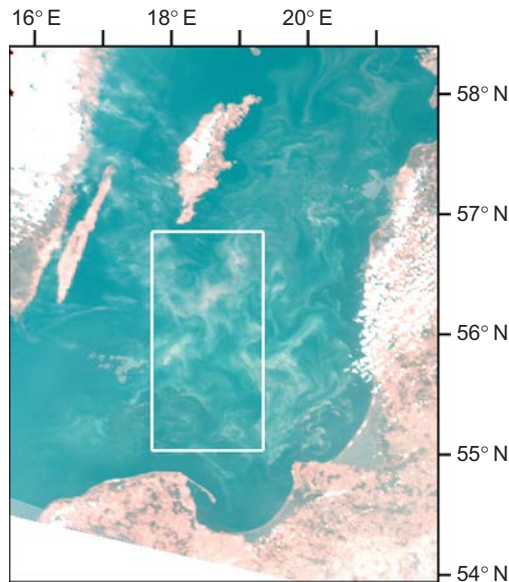
Figure 9. Composite of two SeaWiFS images of the Baltic Proper acquired on 1–2 August, 1999. Image dimensions are 400 km × 250 km. The white square in the centre denotes the (100 km × 200 km) part of the image used for the differential analysis, see text.

4. Discussion

Our results show that various sets of remote-sensing data from satellite-borne sensors working at either the same or different electromagnetic frequencies can be used to derive pixel motions that represent sea surface currents and that manifest in image brightness variations in the used satellite data. Since there are some special aspects that hinder the straightforward use of commonly known motion analysis techniques and algorithms in the area of remote sensing, we used the global motion estimation as a pre-processing step in order to reduce the processing time and to improve the numerical robustness of the differential methods.

We have compared our results with those from operational numerical models run at the Swedish Meteorological and Hydrographic Institute (Sveriges Meteorologiska och Hydrologiska Institut – SMHI; Funkquist and Kleine 2009) and at the German Federal Maritime and Hydrographic Agency (Bundesamt für Seeschifffahrt und Hydrographie, BSH) (Dick *et al.* 2001). We are well aware that *in situ* observations would be best suited for the validation of our results. However, no such (large-scale) *in situ* observations are available for any of the areas of interest and for the dates of satellite acquisitions. Therefore, the available model results have to be taken as the best data to compare our results with. Main characteristics of the two models are briefly summarized in §§4.1 and 4.2.

4.1 *Description of the numerical models*

The BSH circulation model, BSHcmod, is a 48 h forecast model and covers the Baltic Sea and the southern part of the North Sea. In its present form, it is operational since 1999 (Dick *et al.* 2001). Its grid spacing in the Baltic Proper is approximately 10 km
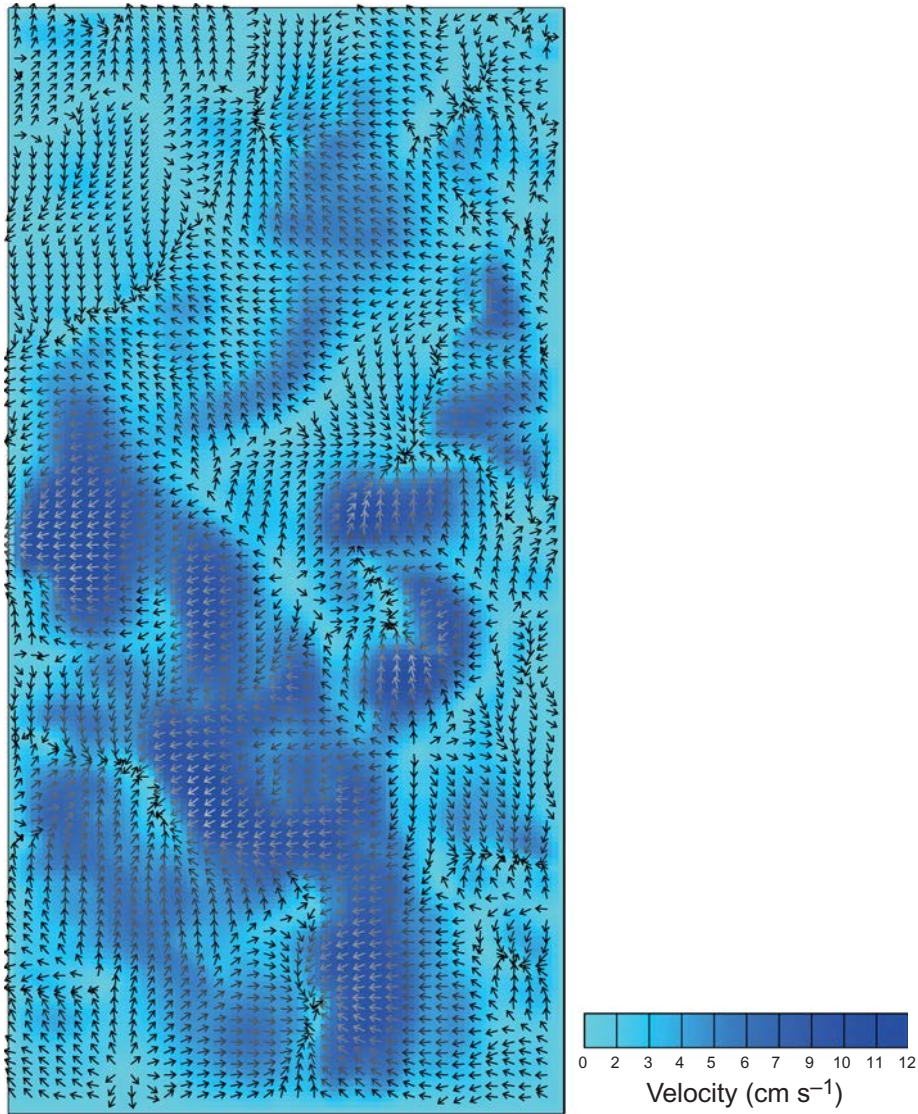
Figure 10. Mean surface currents in the Southern Baltic Sea on 1–2 August, 1999, as derived with the differential method using the pair of SeaWiFS images shown in figure 9. The area dimensions are 100 km × 200 km.

($\Delta\lambda = 10'$, $\Delta\varphi = 6'$). It uses up to 14 vertical layers, of which the first (uppermost) layer is 8 m thick, and time steps of 90 s in the areas presented herein. Meteorological forcing (with forecasts up to 78 h) is provided twice daily through the meteorological forecast model of the German Weather Service (Deutscher Wetterdienst, DWD) and wave forcing through the wave model of DWD. The temporal resolution of the model results is 15 min. For a detailed description of the model skills and validation examples, the reader is referred to Dick *et al.* (2001).

The High-Resolution Operational Model (HIROMB) for the Baltic Sea is based on a previous version of BSHcmod (Funkquist and Kleine 2009). Its grid spacing in

the Baltic Sea is 1 nm (1.852 km). Atmospheric forcing is provided through SMHI's operational atmospheric model (HIRLAM), river runoff forcing through SMHI's operational hydrological model and wind wave forcing from SMHI's wind wave model (HYPAS). It uses up to 24 vertical layers, of which the uppermost has a thickness of 4 m. Model results are provided on a 3 h basis. A more detailed description of HIROMB, along with theoretical background and basic equations can be found in Funkquist and Kleine (2009).

4.2   *Comparison of model results and calculated surface motions*

Example results from each of the models were used to provide a qualitative estimate of the correctness of the surface motions derived from the sequential satellite data. Figure 11 shows model currents of the upper sea layer (0–4 m) on 15 July 1997, at 12:00 UTC, from SMHI's HIROMB model. Inserted in the figure are the areas for which we calculated the surface motions shown in figure 3 (upper right square) and figure 6 (lower left square). The surface motions derived with the MCC method (figure 3) are considerably higher than those provided by the HIROMB model (figure 11), which do not exceed 5 cm s^{-1}. The reason for this difference may be the overall complex current situation during the water inflow from the north, in combination with the impact of the north-easterly wind, which was driving the (very) surface layer towards the southwest. The difference to the results of the BSHcmod (not shown herein) is even larger, and since those data are mean currents in the uppermost eight metres, it is likely that the forcing by the local wind is the reason for the observed differences. Both the NIR and radar sensors image the very sea surface, and thus motions of the very surface layer can only be inferred from the satellite data.

Figure 6 shows a rather complex surface motion field, with a general flow towards the east. This is in general agreement with the HIROMB currents, whereas the model currents are smaller. Again, we note that surface motions derived from satellite data are expected to be larger than mean currents modelled for the upper sea layer (whose thickness is of some metres), when the water surface is mainly driven by the wind.

For the observed oil spills in the Southern Baltic Proper (figure 4), the results of our MCC analyses (figure 5) are in good agreement with the HIROMB model results (figure 12). In both cases, a drift towards the northwest was derived. Moreover, according to HIROMB, the drift of the north-western spill should be (slightly) larger, which was confirmed by our analysis.

The model results from the BSHcmod for the first case of our differential analysis (see figure 6) in the Southern Baltic Proper are shown in figure 13. Our results show a general surface motion towards north (note that the squarish area of interest is rotated), whereas the BSHcmod predicted a mean current of the uppermost 8 m layer towards southeast. At the time of image acquisitions, a moderate wind of 5 m s^{-1} from the south was measured on Hel Peninsula, which apparently forced a northbound surface motion in the area of interest. Apparently this motion can be detected using sequential satellite imagery, whereas it was not strong enough to influence the mean current in the uppermost sea layer.

Finally, figure 14 shows a series of BSHcmod results for 1 August 1999, at 11:00 UTC and 23:00 UTC (upper row) and for 2 August 1999, at 03:00 UTC and 11:00 UTC (lower row). In each of the panels the area is marked, for which a surface motion
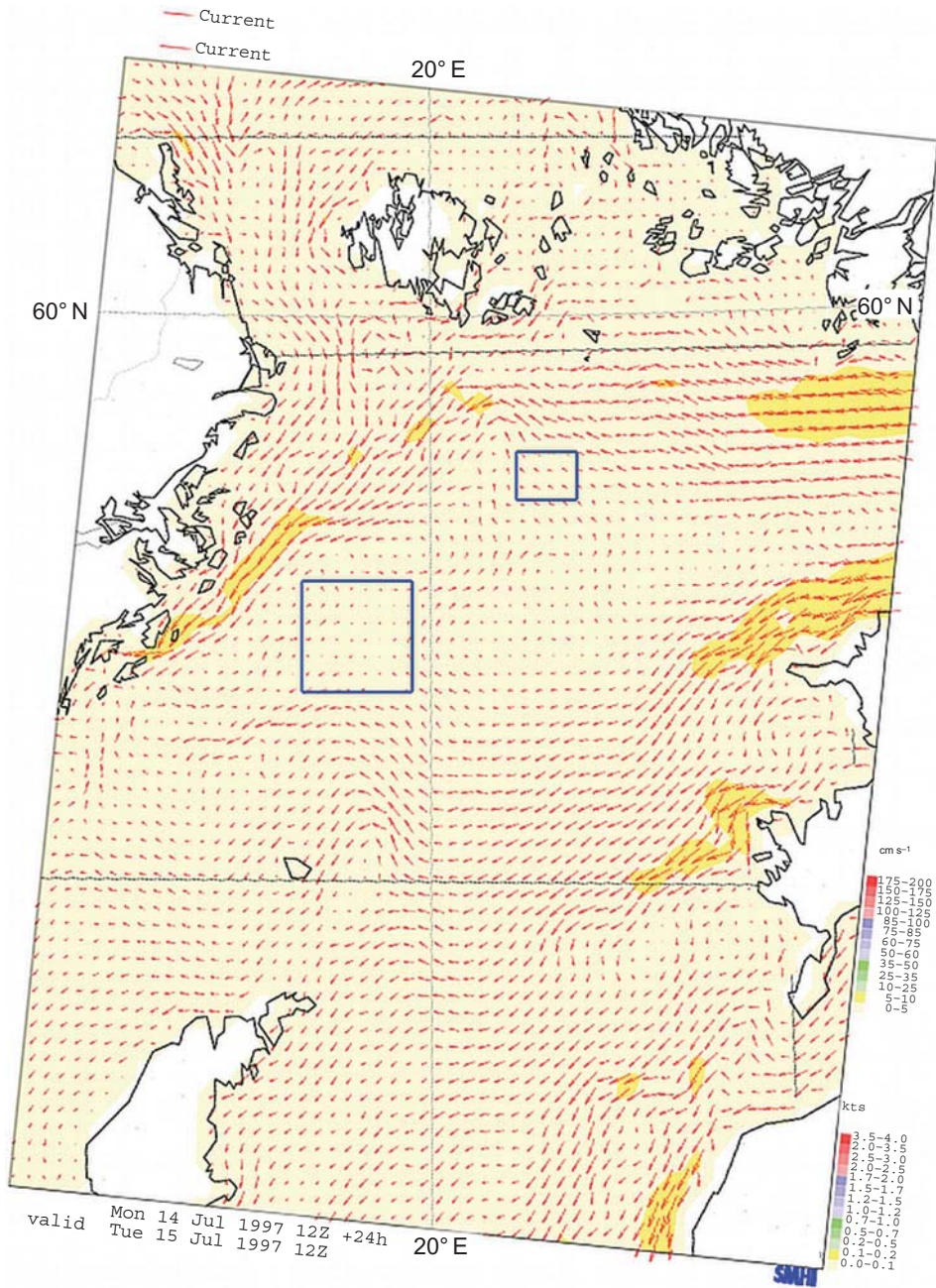
Figure 11. Modelled sea surface currents on 15 July 1997, in the Northern Baltic Proper. Results were obtained with the HIROMB model run at SMHI. The blue squares denote the locations of the areas, for which surface motions were calculated from satellite images.

field was calculated applying the differential method (figure 10). The modelled current field in the uppermost layer (0–8 m) shows some variation in terms of the orientation of the current vectors, but also shows a general westbound current. This is in good
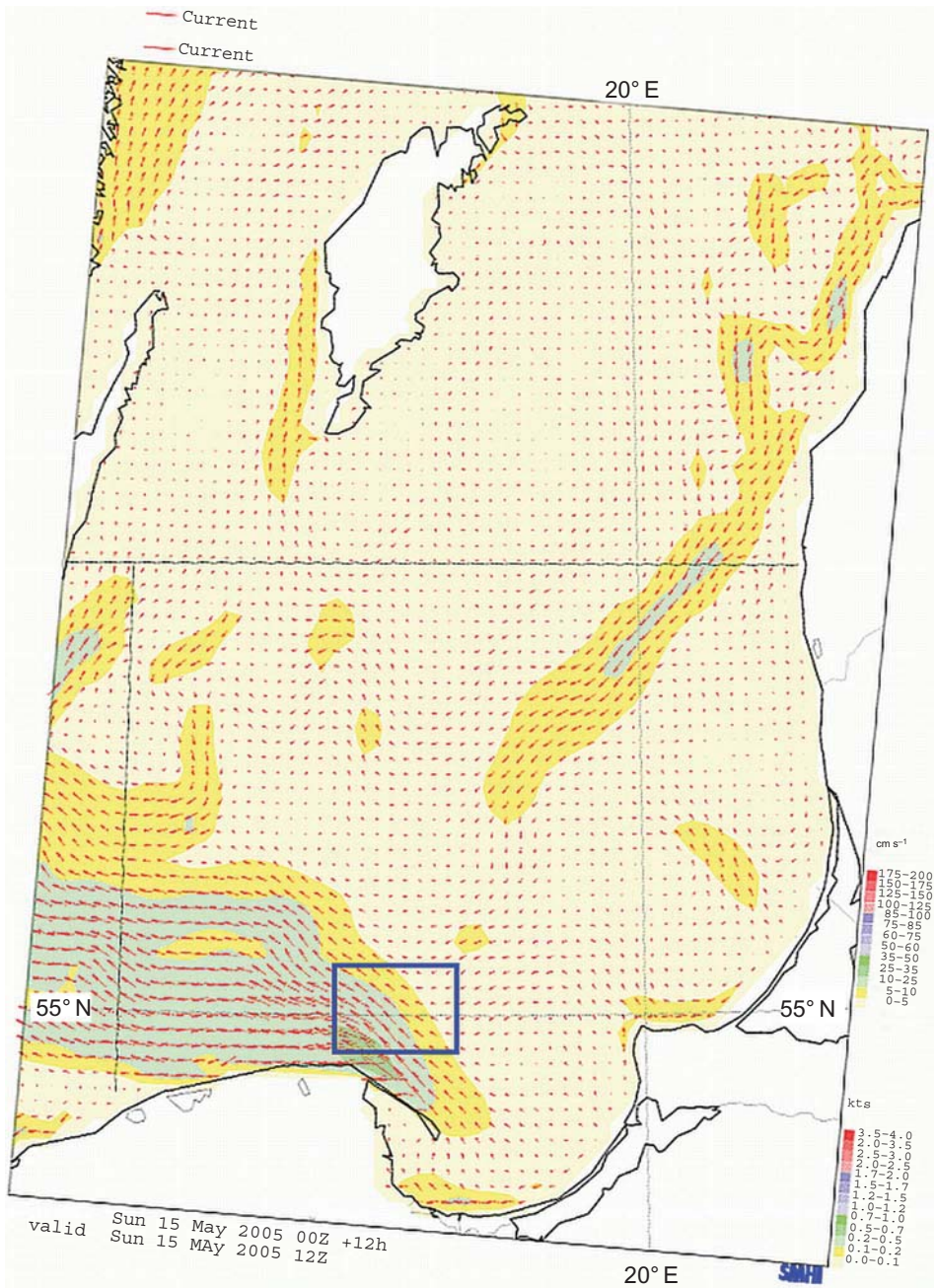
Figure 12. Modelled sea surface currents on 15 May 2005, in the Southern Baltic Proper. Results were obtained with the HIROMB model run at SMHI. The blue square denotes the areas, in which the oil spills were detected, whose motions were calculated from satellite images.

agreement with the results of our differential analysis (figure 10), which implies that low-resolution (1.1 km pixel size) satellite imagery can be used to derive mesoscale surface motion fields with the differential method, for example, using ocean colour data acquired on consecutive days.
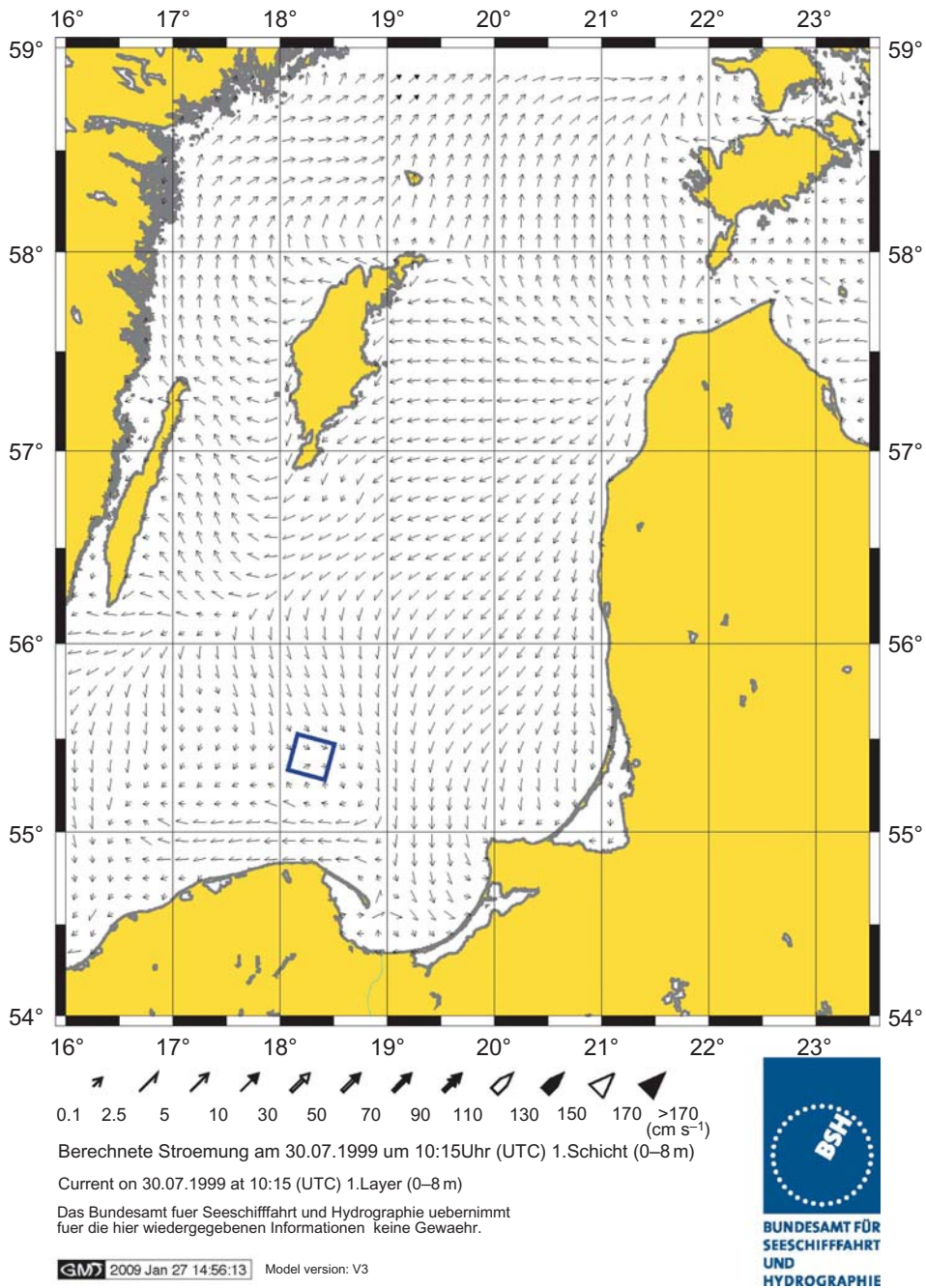
Figure 13. Modelled sea surface currents on 30 July 1999, in the Southern Baltic Proper. Results were obtained with the BSH current model. The inserted square denotes the location of the area, for which surface motions were calculated from satellite images.
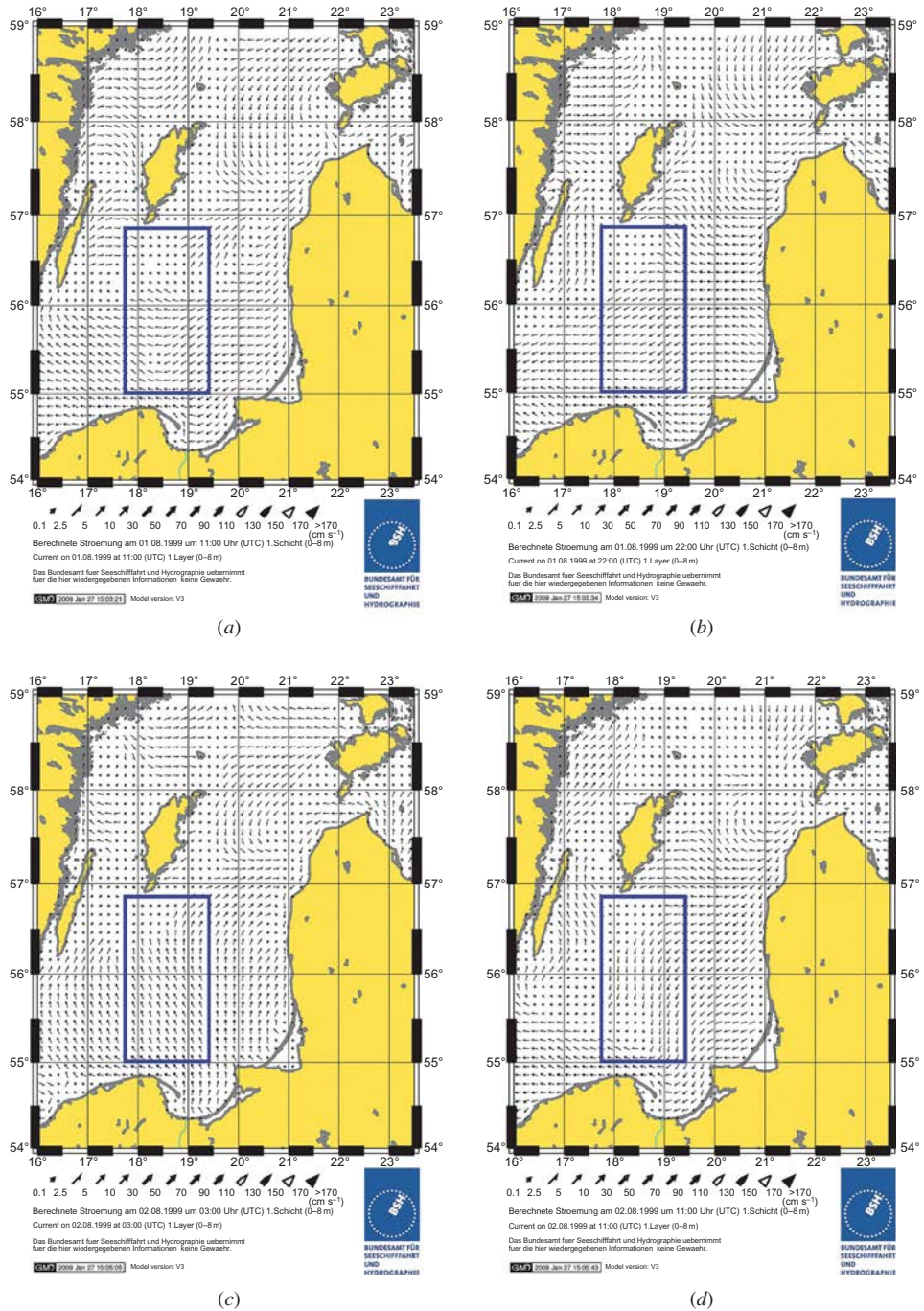
Figure 14. Modelled sea surface currents in the Southern Baltic Proper on 1 August 1999 at (*a*) 11:00 UTC and (*b*) 22:00 UTC; and on 2 August 1999 at (*c*) 03:00 UTC and (*d*) 11:00 UTC. Results were obtained with the BSH current model. The rectangles inserted into each panel denote the area, for which surface motions were calculated from satellite images.

Model data, which represent temporal and spatial means of the local currents, are usually not very well suited for a direct comparison with our results, which represent temporal snapshots at a high spatial resolution. Nonetheless, the comprehensive data set available for the time period of late July/early August 1999, can be used to produce a series of current maps for large parts of the Southern Baltic Proper, which in turn can be compared with available model data. However, we are aware of some limiting factors that need to be considered when series of satellite data are used for current analyses: for example, vertical mixing may hinder a successful calculation of sea surface currents by means of signatures of algae accumulations, and cloud-free weather conditions are generally necessary for this kind of digital image analysis. The effect of the appearance and disappearance of clouds can be seen in figure 6. In this respect, SAR images are advantageous, because they are independent of clouds and daytime.

We note that existing algorithms for the calculation of surface motions are often not well suited to work with remote-sensing data. One weakness is that the normalized MCC algorithm becomes very slow if there is a big spatiotemporal distance between the two used images. This is caused by a quadratically increasing search space of the mask around each observed feature. This fact also influences the differential methods, which assume a quite small spatiotemporal difference between two images. Another problem that has to be taken into account for differential methods is that the internal gradient calculation of these methods may become numerically unstable due to spatial noise and a sparsely populated time axis. Unfortunately, we often encounter such problems when dealing with satellite imagery, where almost every image is noisy and the time axis population often comprises only two images.

5. Conclusions

We have demonstrated that multi-sensor satellite data can be used to compute small-scale pixel motions, if accumulated algae or oil spills are present on the water surface. The two methods applied for this study are a cross-correlation analysis and a differential method based on the Optical Flow algorithm of Horn and Schunck (1981). Because of the different sensor characteristics, the first method was applied using high-resolution imagery (30 m pixel size), whereas the latter was applied using lower-resolution imagery (188 m and 1.1 km pixel sizes). Both methods, however, are not restricted to certain pixel sizes.

Our analyses have shown that sequential satellite imagery from the same or different satellite sensors can be used to derive small to mesoscale surface motion fields. However, caution has to be used when pixel motions are directly converted into sea surface currents, if data from different sensors were used (e.g. TM and WiFS) or if the spatial resolution is too low with respect to the short time lag between the image acquisitions (WiFS). In these cases, we needed to increase the smoothness parameter of the differential method to avoid irregular current patterns. Another problem is the sensitivity of the algorithm to (general) image intensity value changes. Not all image intensity changes result from local surface currents, which in turn is the basic assumption of the differential methods presented herein.

In some cases, two single-channel images acquired, for example, by SAR and NIR sensors, may be sufficient to derive small-scale current fields. However, because of the different imaging of oceanic features by SAR and NIR sensors, this method may fail and the computed currents may be erroneous. Nevertheless, the results shown in figure 3 are likely to represent the real currents, since both NIR sensor and SAR

were detecting algae at the very water surface and the associated damping of surface roughness, respectively (Rud and Gade 1999).

The surface motion fields presented in figures 6, 8 and 10 contain small-scale features that are not resolved in the respective model results. Those features are likely not to be artefacts of the applied image processing techniques, but rather small-scale turbulent features such as ocean surface eddies, which are not resolved by the numerical models. Surface motions derived from satellite data may therefore help investigation of such features, which are often encountered in coastal areas and the understanding of which is crucial for an understanding of coastal ocean dynamics.

Resulting surface current fields, like those presented in this article, may therefore complement model results provided by local hydrographic agencies, particularly since their results were calculated for an upper water layer thickness of some metres and on a much coarser grid (e.g. 4 m depth and a 1 nm grid, respectively, see the available HIROMB data). The use of satellite data, as shown herein, may therefore be a valuable addition to the existing model data.

However, we also encountered limitations of the applied methods due to the different imaging of the observed features (e.g. by SAR and NIR sensors) and due to the different grey level distribution (i.e. sensor sensitivity). Moreover, a limited amount of data or limited visibility of the surface features may also lead to a reduced applicability.

We have also shown that, in some cases, both the optical flow algorithms and the global motion estimation may fail, for example, if there are big spatial and structural changes between the objects of a scene. In these cases, the fast normalized cross-correlation can still yield reliable results.

Acknowledgements

References

ALPERS, W. and HÜHNERFUSS, H., 1988, Radar signatures of oil films floating on the sea and the Marangoni effect. *Journal of Geophysical Research*, **93**, pp. 3642–3648.

BOWEN, M., EMERY, W.J., WILKIN, J.L., TILDESLEY, P., BARTON, I.J. and KNEWTSON, R., 2002, Extracting multi-year surface currents from sequential thermal imagery using the maximum cross correlation technique. *Journal of Atmospheric and Oceanic Technology*, **19**, pp. 1665–1676.

COLLINS, M.J. and EMERY, W.J., 1988, A computational method for estimating sea ice motion in sequential Seasat Synthetic Aperture Radar imagery by matched filtering. *Journal of Geophysical Research*, **93**, pp. 9241–9251.

DICK, S., KLEINE, E., MÜLLER-NAVARRA, S., KLEIN, H. and KOMO, H., 2001, The operational circulation model of BSH (BSHcmod). Model description and validation. *Berichte des Bundesamtes für Seeschifffahrt und Hydrographie*, **29**, p. 48.

EMERY, W.J., FOWLER, C. and CLAYSON, A., 1992, Satellite-image-derived Gulf Stream currents compared with numerical model results. *Journal of Atmospheric and Oceanic Technology*, **9**, pp. 286–304.

EMERY, W.J., THOMAS, A.C., COLLINS, M.J., CRAWFORD, W.R. and MACKAS, D.L., 1986, An objective method for computing advective surface velocities from sequential infrared satellite images. *Journal of Geophysical Research*, **91**, pp. 12865–12878.

ENKELMANN, W., KORIES, R., NAGEL, H.-H. and ZIMMERMANN, G., 1988, An experimental investigation of estimation approaches for optical flow fields. In *Motion Understanding, Robot and Human Vision*, W.N. Martin and J.K. Aggarwal (Eds.), pp. 189–226 (Boston, MA: Kluwer Academic).

FIEDLER, G., 2003, Untersuchungen zur Bestimmung zweidimensionaler Strömungsfelder an der Meeresoberfläche mit Hilfe von multispektralen Satellitenbildern. Diploma thesis, Universität Hamburg, Germany.

FUNKQUIST, L. and KLEINE, E., 2009, An introduction to HIROMB, an operational baroclinic model for the Baltic Sea. Technical report, SMHI, Norrköping, 36 pp. Available online at: http://www.smhi.se/polopoly_fs/1.2135!RO_37%5B1%5D.pdf (accessed 24 February 2011).

GADE, M., ALPERS, W., HÜHNERFUSS, H., MASUKO, H. and KOBAYASHI, T., 1998a, The imaging of biogenic and anthropogenic surface films by a multi-frequency multi-polarization synthetic aperture radar measured during the SIR-C/X-SAR missions. *Journal of Geophysical Research*, **103**, pp. 18851–18866.

GADE, M., FIEDLER, G. and DRESCHLER-FISCHER, L., 2003, Two-dimensional sea surface current fields derived from multi-sensor satellite data. In *IEEE International Geoscience and Remote Sensing Symposium (IGARSS) '03*, 21–25 July 2003, Toulouse, France (Piscataway, NJ: IEEE), pp. 3540–3542.

GADE, M., RUD, O. and ISHII, M., 1998b, Monitoring algae blooms in the Baltic Sea by using optical and microwave sensors. In *IEEE International Geoscience and Remote Sensing Symposium (IGARSS) '98*, 6–10 July 1998, Seattle, WA (Piscataway, NJ: IEEE), pp. 757–759.

GARCIA, C.A.E. and ROBINSON, I.S., 1989, Sea surface velocities in shallow seas extracted from sequential coastal zone color scanner satellite data. *Journal of Geophysical Research*, **94**, pp. 12681–12691.

HORN, B.K.P. and SCHUNCK, B.G., 1981, Determining optical flow. *Artificial Intelligence*, **17**, pp. 185–189.

KAHRU, M., LEPPÄNEN, J.-M. and RUD, O., 1993, Cyanobacterial blooms cause heating of the sea surface. *Marine Ecology Progress Series*, **101**, pp. 1–7.

KAMACHI, M., 1989, Advective surface velocities derived from sequential images for rotational flow field, limitations and applications of maximum cross-correlation method with rotational registration. *Journal of Geophysical Research*, **94**, pp. 18227–18233.

KWOK, R., CURLANDER, J.C., MCCONNELL, R. and PANG, S., 1990, An ice motion tracking system at the Alaska SAR facility. *IEEE Journal of Oceanic Engineering*, **15**, pp. 44–54.

LEWIS, J.P., 1995, Fast template matching. In *Vision Interface '95*, 15–19 June 1995, Quebec, Canada (Ontario: Canadian Information Processing Society), pp. 120–123.

LI, S., CHENG, Z. and WEEKS, W.F., 1998, Extraction of intermediate scale sea ice deformation parameters from SAR ice motion products. In *Analysis of SAR Data of the Polar Oceans: Recent Advances*, C. Tsatsoulis and R. Kwok (Eds.), pp. 69–90 (New York: Springer).

LIU, A.K., ZHAO, Y. and HSU, M.-K., 2006, Ocean surface drift revealed by synthetic aperture radar images. *Electro Optical System*, **87**, pp. 233–239.

LUCAS, B.D. and KANADE, T., 1981, An iterative image registration technique with an application to stereo vision. In *7th International Joint Conference on Artificial Intelligence (IJCAI) '81*, April 1981, Vancouver, Canada, (San Francisco, CA: Morgan Kaufmann), pp. 674–679.

RUD, O. and GADE, M., 1999, Monitoring algae blooms in the Baltic Sea, a multisensor approach. In *Oceans '99*, September 1999, Seattle, WA (Piscataway, NJ: IEEE), pp. 1234–1238.

RUD, O. and GADE, M., 2000, Using multisensor data for algae bloom monitoring. In *IEEE International Geoscience and Remote Sensing Symposium (IGARSS) '00*, 24–28 July 2000, Honolulu, HI (Piscataway, NJ: IEEE), pp. 1714–1716.

SUN, Y., 1996, Automatic ice motion retrieval from ERS-1 SAR images using the optical flow method. *International Journal of Remote Sensing*, **17**, pp. 2059–2087.

TOKMAKIAN, R., STRUB, T.P. and MCCLEAN-PADMAN, J., 1990, Evaluation of the maximum cross-correlation method of estimating sea surface velocities from sequential satellite images. *Journal of Atmospheric and Oceanic Technology*, **7**, pp. 852–865.